Journal of Energy Chemistry 55 (2021) 355–360

Contents lists available at ScienceDirect

Journal of Energy Chemistry

journal homepage: www.elsevier.com/locate/jechem

http://www.journals.elsevier.com/journal-of-energy-chemistry/

3D star-like atypical hybrid MOF derived single-atom catalyst boosts oxygen reduction catalysis

Lei Zhou [a,b], Peng Zhou [b], Yelong Zhang [c], Bingyao Liu [d], Peng Gao [d], Shaojun Guo [a,b,*]

[a] BIC-ESAT, College of Engineering, Peking University, Beijing 100871, China
[b] Department of Materials Science and Engineering, College of Engineering, Peking University, Beijing 100871, China
[c] School of Applied Physics and Materials, Wuyi University, Jiangmen 529020, Guangdong, China
[d] International Center for Quantum Materials, and Electron Microscopy Laboratory, School of Physics, Peking University, Beijing 100871, China

ARTICLE INFO

Article history:
Received 22 April 2020
Revised 24 June 2020
Accepted 24 June 2020
Available online 9 July 2020

Keywords:
Single atom catalysts
Oxygen reduction reaction
Metal-organic frameworks
Zn-air battery

ABSTRACT

Developing high-efficiency, stable and non-precious electrocatalysts for oxygen reduction reaction (ORR) is highly important for energy conversion and storage. Single atom catalysts (SACs) show good potential in enhancing ORR, however, the specifical control over the coordination surroundings around single metal center to intrinsically modify the electron structure is still a great challenge. Herein, we demonstrate that a 3D hybrid MOF composed of cobalt doped ZIF-L and ZIF-8, featuring star morphology with six equal branches, can be used as an advanced precursor for making the Co SACs for greatly boosted ORR. The as-synthesized Co_{SA}-N-C exhibits excellent ORR activity with $E_{1/2}$ of 0.891 V in alkaline medium, outperforming the commercial Pt/C by 39 mV. Moreover, the $E_{1/2}$ of Co_{SA}-N-C (0.790 V) is merely 15 mV, less than that of Pt/C (0.805 V) in acid medium, which is among the best in the reported state-of-the-art SACs. DFT calculations demonstrate that the enhanced ORR performance is assigned to the formation of atomically isolated cobalt atom coordinated three N atoms and one C atom, which is easier to decrease the free energy of rate determining step and accelerate the ORR process than that of traditional cobalt atom coordinated four N atoms. In addition, a primary Zn-air battery with Co_{SA}-N-C cathode reveals a maximum power density of 92.2 mW cm^{-2} at 120.0 mA cm^{-2}, far higher than that of commercial catalysts (74.2 mW cm^{-2} at 110.0 mA cm^{-2}).

1. Introduction

Proton exchange membrane fuel cells (PEMFCs) have become the promising candidate for future automotive applications due to their high efficiency and zero carbon emission [1–4]. However, their large-scale commercialization of PEMFCs is severely hindered by the sluggish kinetics of oxygen reduction reaction (ORR) and the prohibitive cost of noble-metal catalyst at cathode. Extensive efforts have been devoted to designing non-precious metal ORR electrocatalysts with enhanced activity and stability, such as metal-free heteroatom-doped carbon [5–8], transition metal carbides or nitrides [9–12], and transition metal coordinated complexes [13–16]. Recently, single atom catalysts (SACs) have emerged as a new alternative in heterogeneous catalysis, such as CO oxidation [17–20], CO_2 reduction [21–23], water splitting [24–26], ORR [27–29] and organic synthesis [30]. Typically, the catalytically active metal sites are often coordinated by nitrogen/oxygen/carbon atoms and atomically dispersed on a solid support. Among these SACs, transition metal and nitrogen co-doped carbon (M–N–C) materials have attracted great attention owing to their good electrocatalytic activity, satisfying stability, and maneuverable scale-up production [31–34]. The MN*x* moieties distributed in the basal planes of carbon matrixes, resembling to the metal-macrocycle complexes, are regarded as active sites for catalyzing ORR. Compared with their bulk counterparts (nanoparticles or clusters), SACs with unique electronic structure can expose the most active sites and maximize the efficiency of atom utilization, which is beneficial to boost the specific electrocatalytic performance [35,36]. In addition, the electronic structure of single metal atom centers can be precisely tuned by altering the anchoring coordination atoms in the supporting substrates, which can further modify the corresponding electrocatalytic activities. Despite considerable efforts have been devoted to fabricating carbon-based SACs *via* pyrolysis of metal-organic frameworks (MOFs) with

* Corresponding author at: BIC-ESAT, and Department of Materials Science and Engineering, College of Engineering, Peking University, Beijing 100871, China.
E-mail address: guosj@pku.edu.cn (S. Guo).

https://doi.org/10.1016/j.jechem.2020.06.059
2095-4956/

enhanced ORR activities, attention has rarely been paid to tuning the coordination atom numbers and species of metal centers in single-atom materials to enhance the ORR performance.

Herein, we report a new 3D star-like mixed-MOF containing Co doped ZIF-8 and ZIF-L that can be used as a new precursor for constructing single atom catalyst (Co_{SA}-N-C) with unique Co-N_3C coordination, which is different from the traditional SACs with Co-N_4 coordination derived from ZIF-8 precursors. The as-synthesized Co SACs display highly efficient ORR activity with a half-wave potential ($E_{1/2}$) of 0.891 V *vs.* reversible hydrogen electrode (RHE) in 0.1 M KOH, 39 mV more positive than that of the commercial Pt/C (0.852 V *vs.* RHE). Moreover, it also exhibits the satisfying ORR activity in acid medium with $E_{1/2}$ of 0.790 V *vs.* RHE, merely 15 mV less than that of Pt/C (0.805 V *vs.* RHE), which is among the best single-atom catalysts that have been reported. First-principle calculations reveal that the Co-N_3C coordination can create a new electronic state near the Fermi level to hybrid with oxygen molecule and significantly decrease the free energy of rate determining step compared with Co-N_4 and Co nanoparticle, thus boosting the ORR performance. Besides, a Co_{SA}-N-C cathode Zn–air battery displays a maximum power density of 92.2 mW cm^{-2} at 120.0 mA cm^{-2}, far higher than that of commercial catalysts (74.2 mW cm^{-2} at 110.0 mA cm^{-2}). Our work opens up a new routine for the controllable synthesis of efficient single atom catalysts toward energy storage and conversion.

2. Experimental

2.1. Preparation of star-like MOF precursors

In a typical procedure, $Zn(NO_3)_2{\cdot}6H_2O$ (0.594 g), cetyltrimethylammonium bromide (CTAB) (10 mg) and certain amount of Co $(NO_3)_2{\cdot}6H_2O$ (0, 29 and 290 mg) were dissolved in 20 mL deionized water, and stirred to form a clear solution (solution A). Meantime, 2-methylimidazole (MeIM) (4.5 g) was dissolved in 80 mL deionized water and stirred to form a clear solution (solution B). Subsequently, the solution A was quickly poured into solution B, and then stirred under room temperature for 3 h, producing the pink precipitate after 10 min. The precipitate was centrifuged with distilled water and ethanol for three times, and dried at 60 °C for 6 h. ZIF-L is a two-dimensional layered Zeolitic Imidazolate Framework (ZIF) consists of Zn metal ions and 2-methylimidazole (2-MeIm) molecules, which are the same building blocks as ZIF-8. Unlike ZIF-8, the two neighboring two-dimensional layers in ZIF-L are bridged by hydrogen bonds instead of 2-MeIm molecules.

2.2. Preparation of Co_0-N-C, Co_{SA}-N-C and Co_{NP}-N-C

The Co_0-N-C, Co_{SA}-N-C and Co_{NP}-N-C were prepared by the temperature-programmed procedure. The power of star-like MOF precursors was transferred into a ceramic boat and placed in a tube furnace. The sample was heated to 910 °C with a heating rate of 5 °C min^{-1} and kept at 910 °C for 2 h under flowing argon gas and then naturally cooled to room temperature.

2.3. Characterization

X-ray diffraction patterns were collected on a Shimadzu XRD-6000 diffractometer using a Cu K_α source, with a scan step of 0.02° and a scan range between 5° and 80°. The morphology of the as prepared materials was investigated using a scanning electron microscope (SEM; Zeiss SUPRA 55) with an accelerating voltage of 20 kV. Transmission electron microscopy (TEM) images were recorded with Philips Tecnai 20 and JEOL JEM-2010 high-resolution transmission electron microscopes. High-resolution TEM (HRTEM) and high-angle annular dark-field scanning TEM (HAADF-STEM) images were collected on a FEI Tecnai G2 F20 S-Twin working at 200 kV. The relative energy-dispersive X-ray spectrometry (EDS) elemental mapping in the STEM were operated with a probe focused to 0.2 nm and camera length of 20 cm. X-ray photoelectron spectra (XPS) were performed on a Thermo VG ESCALAB 250 X-ray photoelectron spectrometer at a pressure of about 2×10^{-9} Pa using Al K_α X-ray as the excitation source. The atomic-resolution HAADF-STEM and Electron energy loss spectroscopy measurements were carried out from monochromatic Nion-HERME200 at 60 kV.

3. Results and discussion

The synthesis process for the novel Co SACs electrocatalyst is shown in Fig. 1(a). Firstly, a uniformly star-like hybrid MOF consists of ZIF-L and ZIF-8, which is confirmed by XRD (Fig. S1), has been fabricated as an advanced precursor. Meanwhile, partial Zn^{2+} sites were replaced by Co^{2+} through adding certain amount of cobalt nitrate. After pyrolysis at 910 °C under N_2 atmosphere, the hybrid MOF was transformed into nitrogen doped porous carbon. Simultaneously, due to the uniformly dispersed Co atoms separated by Zn atoms in hybrid MOF precursor, the aggregation of Co single atoms into clusters or particles can be efficiently avoided. Owing to the lack of MeIm ligand between the layers in ZIF-L relative to that of ZIF-8, the Co single atoms derived from hybrid MOF were structured by Co-N_3C instead of Co-N_4. As a result, the isolated Co-N_3C moieties were uniformly anchored on nitrogen doped carbon frameworks. In a similar way, a series of Co_x-N-C have been prepared by changing the added cobalt amount in MOF precursors, including Co_0-N-C (no cobalt), Co_{SA}-N-C (moderate cobalt) and Co_{NP}-N-C (excessive cobalt).

The morphologies of the catalysts before and after pyrolysis were firstly studied by scanning electron microscopy (SEM) and transmission electron microscopy (TEM). As shown in

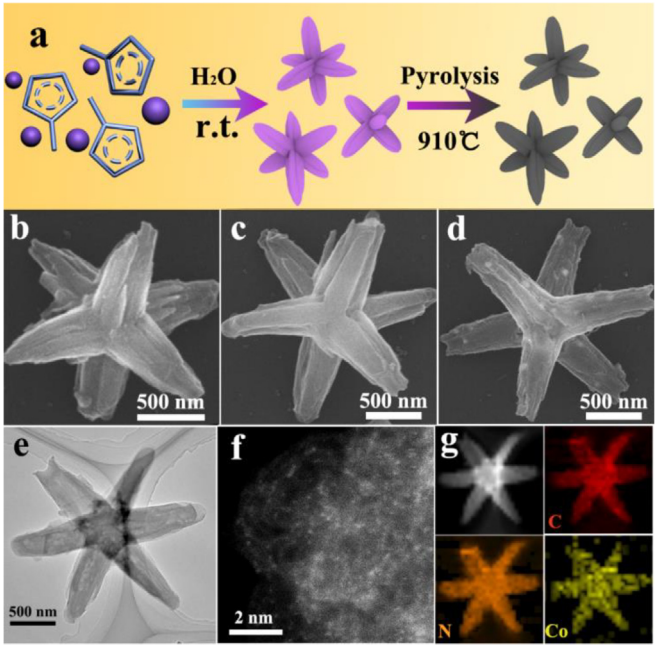

Fig. 1. (a) Schematic illustration for synthesis of Co_{SA}-N-C star-like catalysts. SEM images of (b) Co_0-N-C, (c) Co_{SA}-N-C and (d) Co_{NP}-N-C, respectively. (e) TEM image and (f) atomic-resolution HAADF-STEM image of the Co_{SA}-N-C. (g) The corresponding elemental mappings show the distribution of Co (yellow), C (red), and N (orange).

Figs. S2–S4, all the MOF precursors show the regular star shape with six equal branches, and Co atoms are successfully incorporated into the whole architecture. After the pyrolysis treatment in N_2 atmosphere, the Co_{SA}-N-C retains its initial nanostructure, while its surface becomes much rougher (Fig. 1(c)). As displayed in Fig. 1(d), some cobalt nanoparticles were obviously existed inside the carbon frameworks in Co_{NP}-N-C. According to the TEM result (Fig. 1(e)), no cobalt nanoparticles were observed in the Co_{SA}-N-C. Atomic-resolution high-angle annular dark-field scanning transmission electron microscopy (HAADF-STEM) analysis was carried out to further investigate the Co_{SA}-N-C at atomic level. Fig. 1(f) shows that Co single atoms were atomically dispersed on the porous carbon frameworks, identified by isolated bright dots marked with yellow cycles. Furthermore, the elemental mapping and electron energy loss spectroscopy (EELS) results show that Co, C, and N are uniformly distributed throughout the entire nanostructure (Figs. 1(g) and S5). In addition, the HRTEM and Brunauer–Emmett–Teller (BET) results reveal the mesoporous feature of Co_{SA}-N-C with a large surface area of 570 m^2 g^{-1} and an average pore size of 4.37 nm, which is benefit to expose more catalytic sites for oxygen adsorption and reaction (Figs. S6 and S7).

The X-ray diffraction (XRD) was performed to confirm the crystal structure of the as-prepared catalysts. As displayed in Fig. 2(a), the Co_{SA}-N-C shows broad and weak diffraction at around 25° and 43° in the XRD pattern, the same as that of Co_0-N-C. The peaks are assigned to (002) and (101) planes of the graphitic carbon, further confirmed by Raman spectra (Fig. S8). No peaks of cobalt nanoparticles or oxides are detected in Co_{SA}-N-C, indicating the Co species are dispersed at atomic scale. X-ray photoelectron spectroscopy (XPS) was conducted to further investigate the surface chemical composition and state of the Co_{SA}-N-C. The survey spectrum of Co_{SA}-N-C indicates the presence of Co, C, N and O (Fig. S9). High-resolution N 1 *s* spectrum can be deconvoluted into four characteristic peaks, corresponding to pyridinic (398.5 eV), Co-N*x* (399.2 eV), pyrrolic (400.3 eV) and graphitic (401.2 eV) nitrogen species, which serve as the potential sites for anchoring cobalt atoms (Fig. 2(b)). The C 1 *s* spectrum shows the existence of C—N and C═N bonds, implying the Co-N*x* moieties successfully disperse in the carbon framework (Fig. S10). In addition, the Co-C bond is also displayed in C 1 *s* spectrum, suggesting that the co-existence of Co-C and Co-N coordination around the single cobalt active centers. The two characteristic peaks at 796.2 and 780.7 eV are attributed to $2p_{3/2}$ and $2p_{1/2}$ peaks of Co 2*p* (Fig. S11), in accordance with reported Co-C*x*N*y* structure [37]. The Co content was about 2.5 wt %, confirmed by inductively coupled plasma optical emission spectrometry (ICP-OES), STEM-EDS and thermogravimetric analysis (TGA) analysis (Figs. S12, S13 and Tables S1, S2).

To confirm the structure of Co_{SA}-N-C at atomic level, X-ray absorption near-edge structure (XANES) and extended X-ray absorption fine structure (EXAFS) were carried out. As shown in Fig. 2(c), FT-EXAFS curve for Co_{SA}-N-C only shows a major peak at about 1.4 Å, attributed to Co–N(C) scattering path, and the Co–Co peak at about 2.2 Å was not detected. A least-squares EXAFS fitting was carried out to obtain the quantitative structural parameters of Co in the Co_{SA}-N-C. The EXAFS fitting parameters and fitting curves were displayed in Table S3 and Fig. 2(d), respectively. The coordination number of Co was about 4, in which one Co atom was coordinated by three N atoms and one C atom. In order to exclusively identify the Co-N_3C structure in Co_{SA}-N-C, the cobalt phthalocyanine (CoPc) is included as reference for comparison. The scattering peak for CoPc with typical Co-N_4 coordination is at approximately 1.48 Å, which is larger than that of Co-N_3C in

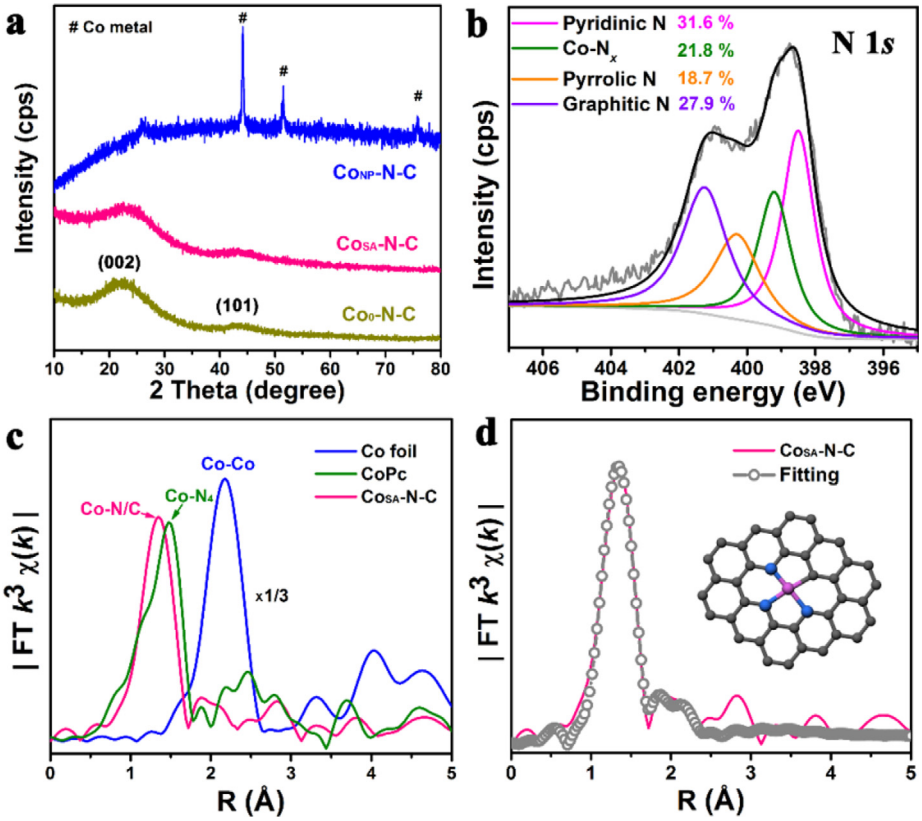

Fig. 2. (a) XRD patterns of Co_0-N-C, Co_{SA}-N-C and Co_{NP}-N-C. (b) N 1 *s* XPS spectrum of the Co_{SA}-N-C. (c) Fourier transform (FT) of the Co *K*-edge for Co_{SA}-N-C, CoPc and Co foil. (d) The corresponding EXAFS *R* space fitting curves of Co_{SA}-N-C. Inset: schematic model of Co_{SA}-N-C, Co (pink), N (blue) and C (gray).

Co_{SA}-N-C. The shorter length of Co_{SA}-N-C is probably due to the contracted structure of Co-C compared with Co-N coordination. As illustrated in the inset of Fig. 2(d), the atomic structure model shows the tetra-coordinated Co atom is atomically anchored in the nitrogen-doped porous carbon matrix. Unlike the most reported Co single atom catalysts derived from modified ZIF-8, Co_{SA}-N-C exhibits a unique coordination with one C and three N atoms, instead of the common four N atoms. It is inferred that the low ligand ratio in ZIF-L in hybrid MOFs compared with pure ZIF-8 crystals leads to insufficient N coordination for Co_{SA}-N-C.

The electrochemical performance of Co_{SA}-N-C towards ORR was evaluated in an alkaline medium with rotating disk electrode (RDE) measurement. Fig. 3(a) shows the CV curves of a series of Co_x-N-C catalysts in O_2-saturated (solid line) and N_2-saturated (dashed line) 0.1 M KOH. The CV curves of Co_0-N-C without Co doping exhibits a much lower oxygen reduction peak than those of Co_{SA}-N-C and Co_{NP}-N-C, suggesting the indispensable role of Co sites in enhancing ORR activity. Fig. 3(b) exhibits the polarization curves of various samples and commercial Pt/C catalyst (20 wt%) obtained at a rotating speed of 1600 rpm. Linear sweep voltammetry (LSV) curves indicate the best performance of Co_{SA}-N-C among all related catalysts, featuring a higher half-wave potential ($E_{1/2}$ = 0.891 V *vs*. RHE) than Co_0-N-C (0.775 V *vs*. RHE), Co_{NP}-N-C (0.870 V *vs*. RHE), and the commercial Pt/C (0.852 V *vs*. RHE) (Fig. S16).

To gain more insight into the electron-transfer mechanism of Co_{SA}-N-C, LSV measurements were recorded at different rotating speed (Fig. 3(d)). The K-L plots obtained from the LSV curves exhibit excellent linearity, implying the first-order reaction kinetics for ORR with a potential-independent electron transfer rate (Fig. 3(d) inset). According to the K-L equation, the electron transfer number is determined to be about 3.9, demonstrating the four-electron transfer ORR mechanism for Co_{SA}-N-C. Moreover, rotating ring disk electrode (RRDE) was conducted to further investigate the ORR performance of Co_{SA}-N-C. As shown in Fig. S17, Co_{SA}-N-C shows a very low (<5.4%) H_2O_2 yields with the electron transfer number larger than 3.9, in accordance with the results of K-L plots. Moreover, Co_{SA}-N-C exhibits excellent durability with only about 6 mV decay after 6000 cycles, attributed to the strong affinity between atomic Co sites and coordinated N atoms (Fig. 3(e)). Furthermore, Co_{SA}-N-C also displays the promising performance in 0.1 M $HClO_4$. As showed in Figs. S18 and S19, Co_{SA}-N-C exhibits an obviously oxygen reduction peak at 0.72 V *vs*. RHE, much positive than that of Co_0-N-C (0.41 V *vs*. RHE), indicating the important role of catalytic center for the isolated Co atoms. Furthermore, as shown in Fig. 3(c), the Co_{SA}-N-C exhibits the half-wave potential of 0.790 V *vs*. RHE, merely 15 mV less than that of Pt/C (0.805 V *vs*. RHE), which is among the best ORR catalysts in acid electrolyte (Table S4). In addition, after the current–time (*i-t*) chronoamperometry measurements at constant potential (0.3 V vs. RHE) for 10 h, the current density only displayed ~ 12% decay, indicating the good stability of the Co_{SA}-N-C in acid media (Fig. S21).

The electrochemical impedance spectra (EIS) test was carried out to gain a further insight into the abilities of electrons transportation of as-obtained samples. As displayed in Fig. S22, the semicircles in the Nyquist plot for Co_{SA}-N-C is much smaller than those of Co_0-N-C and Co_{NP}-N-C, illustrating the substantially lower charge-transfer resistance of Co_{SA}-N-C. Moreover, the electrochemical active surface area (ECSA) was estimated on the basis of the electrochemical double-layer capacitance (C_{dl}). As displayed in Fig. S23, the Co_0-N-C, Co_{SA}-N-C and Co_{NP}-N-C exhibit similar C_{dl}, demonstrating that the amount of exposed active sites is not the predominated reason account for the enhanced ORR activity of Co single atom catalysts.

To explore the nature of the high ORR activity of Co_{SA}-N-C, density functional theory (DFT) calculations were carried out to further investigate the role of isolated Co centers in tuning electronic structure and modifying the energy change in ORR process. According to the experimental and reported results, the isolated Co coordinated with one C and three N atoms, and Co (101) surface were adopted as the active sites of Co_{SA}-N-C and Co particles for

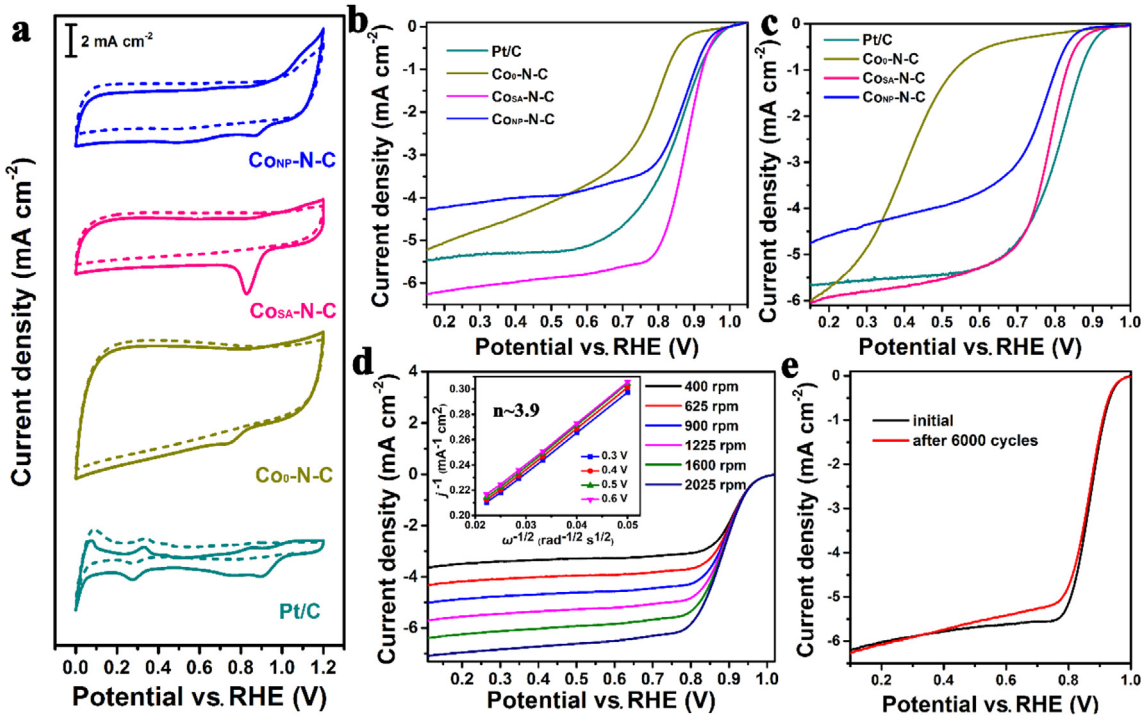

Fig. 3. (a) CV curves of Co_0-N-C, Co_{SA}-N-C, Co_{NP}-N-C and Pt/C in O_2-saturated (solid lines) and N_2-saturated (dashed lines) in 0.1 M KOH at a sweep rate of 50 mV s^{-1}. The corresponding LSV curves were recorded in (b) O_2-saturated 0.1 M KOH and (c) 0.1 M $HClO_4$ at 1600 rpm. (d) ORR polarization curves at different rotating speeds (inset: K-L plots and electron transfer numbers); (e) ORR polarization curves of Co_{SA}-N-C before and after 6000 cycles.

ORR, respectively (Fig. S24). To further clearly reveal the detailed coordination structure for Co_{SA}-N-C, the calculation model is named as Co-N_3C. As demonstrated by the density of states (DOS) of Co 3d in Co-N_3C (Fig. S25), a new hybridized electronic state emerged near the Fermi level compared with Co nanoparticle. This new electronic state could be ascribed to the strong interaction between Co and the neighbor coordinated atoms (C or N atoms), which is beneficial to the orbital hybridization between the O 2*p* and Co 3*d*. The free-energy paths of Co-N_3C and Co nanoparticle are shown in Fig. 4(a and b), and the detail reaction energetics are listed in Table S5. Typically, the ORR process involves such four-electron elementary steps:

$$O_2^* + H^+ + e^- \rightarrow OOH^* \quad (1)$$

$$OOH^* + H^+ + e^- \rightarrow O^* + H_2O \quad (2)$$

$$O^* + H^+ + e^- \rightarrow OH^* \quad (3)$$

$$OH^* + H^+ + e^- \rightarrow H_2O^* \quad (4)$$

where * indicates the reactive sites and the OOH*, O*, OH* are adsorbed intermediates. As shown in Fig. 4(a), all the electron-transfer steps are exothermic for Co-N_3C, leading to a downhill free energy pathway when $U = 0$ V. However, there is an energy barrier (0.36 eV) at third step for Co nanoparticle, indicating more external energy is needed to drive the reduction of *O to *OH in comparison to Co-N_3C. Moreover, when the potential increases to 1.23 V, both the first and third electron transfer step was endothermic (Fig. 4 (b)). According to the free energy of four electron transfer step, the rate determining step (RDS) was predicted to the third reduction step for both Co-N_3C and Co nanoparticle, determined by the highest endothermic energy during the whole process. As a result, the free energy at RDS is 0.63 eV for Co-N_3C, much lower than 1.60 eV for the Co nanoparticle, suggesting the enhanced intrinsic activity of Co single atoms compared with particles from the perspective of thermodynamics. This is considered from the reason that the orbital hybridization between the O 2*p* and Co 3*d* in Co-N_3C enhances the electron-captured ability of Co center. These results demonstrate that ORR activity can be greatly boosted *via* downsizing the Co particles to single atoms, which was achieved by efficient reducing the activation energy barrier of RDS. Furthermore, the active sites structure for most MOF derived single atom catalysts is one metal atom coordinated by four nitrogen atoms. Thus, the free energy changes of ORR reaction process on four nitrogen coordinated cobalt (Co-N_4) have also been calculated for a comparison. As shown in Fig. 4(a), the Co-N_4 exhibits the similar energy change with Co-N_3C, which means thermodynamic favor when $U = 0$ V. However, when potential was applied up to 1.23 V, the activation energy barrier for Co-N_4 is 0.94 eV to drive the reduction of *OOH to *O, much larger than that of Co-N_3C (Fig. 4(b)). In addition, the RDS for Co-N_4 is reducing *OOH to *O instead of *O to *OH for Co-N_3C, which indicates that replacing one coordinated nitrogen atom with carbon atom can alter the reaction process and reduce activation energy barrier, thus promoting the ORR performance.

Motivated by the outstanding electrocatalytic performance of Co_{SA}-N-C, the application of Co_{SA}-N-C in advanced battery system was further assessed under real operation conditions. A home-made primary Zn-air battery was assembled with a Co_{SA}-N-C air cathode, an alkaline electrolyte (6.0 M KOH + 0.2 M $ZnCl_2$), and a Zn plat anode (Fig. S26). For a comparison, the performance of commercial Pt/C catalyst was also tested under the same measurement conditions. The Co_{SA}-N-C battery achieves a specific capacity of 634.2 mAh g^{-1} with a gravimetric energy density of 728.4 Wh kg_{Zn}^{-1}, higher than those of the commercial battery (specific capacity of 557.6 mAh g^{-1} and energy density of 622.5 Wh kg_{Zn}^{-1}, Fig. S27). Moreover, the discharge polarization and power density curves (Fig. 4(c)) clearly shows that the Co_{SA}-N-C cathode gives larger current density and peak power density than those commercial battery. Notably, the Co_{SA}-N-C battery reveals a maximum power

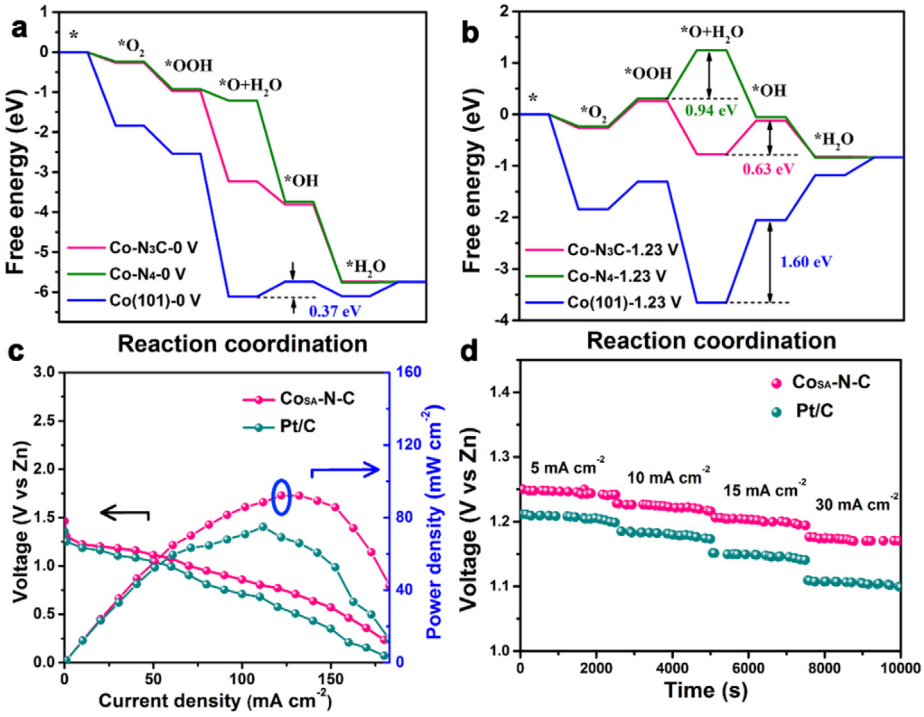

Fig. 4. Free energy paths of ORR on Co-N_3C, Co-N_4 and Co nanoparticles at (a) $U = 0$ V and (b) $U = 1.23$ V. (c) Polarization and power density curves of primary Zn-air batteries using Co_{SA}-N-C and commercial Pt/C as ORR catalysts and 6 M KOH as electrolyte. (d) Galvanostatic discharge curves at different current densities based on Co_{SA}-N-C and commercial Pt/C cathode, respectively.

density of 92.2 mW cm^{-2} at 120.0 mA cm^{-2} far higher than those of commercial catalysts (74.2 mW cm^{-2} at 110.0 mA cm^{-2}). The voltage plateaus of the Co_{SA}-N-C at different current densities (from 5 to 30 mA cm^{-2}) in the galvanostatic discharge process are also higher than those from the commercial counterpart (Fig. 4(d)), making it highly promising for both high-energy densities and high-power capabilities applications [38–40]. Moreover, a commercial LED device can be easily illuminated with no obvious decrease in brightness over 1 h by connecting two Co_{SA}-N-C-based Zn–air batteries in series (Fig. S28), demonstrating a significant potential application [41–43].

4. Conclusions

In summary, a novel 3D Co based single atom catalyst (Co_{SA}-N-C) with a unique star-like morphology and Co-N_3C coordination structure has been successfully designed and fabricated. The Co_{SA}-N-C inherits the six-equaled branches morphology of the hybrid MOF precursors, which provide abundant active sites for directly connecting to the reactants in electrolyte. Moreover, thanks to the special ratio of metal and ligand in hybrid MOF precursors, the electrochemical active Co-N_3C moieties can atomically disperse in the N-doped carbon substrate. As a result, the Co_{SA}-N-C catalyst exhibits excellent ORR catalytic activity and electrochemical stability in oxygen reduction and primary Zn – air batteries. Furthermore, the DFT calculations reveals that the unique Co-N_3C coordination in Co_{SA}-N-C leads to a new electronic state to hybrid with oxygen molecule and significantly decreases the free energy barrier of rate determining step in ORR compared with four nitrogen coordinated Co (Co-N_4) single atom and Co particle catalysts. Furthermore, the Co_{SA}-N-C as cathode reveals satisfying performance in Zinc-air battery, which shows promising potential in energy storage and conversion fields.

Declaration of Competing Interest

The authors declare that they have no known competing financial interests or personal relationships that could have appeared to influence the work reported in this paper.

Acknowledgments

This work was financially supported by the National Natural Science Foundation of China (NSFC) (21802003, 51672007, 11974023), the China Postdoctoral Science Foundation (No. 2019M650337), and the Science Foundation for High-Level Talents of Wuyi University, China (2018RC50).

Appendix A. Supplementary data

Supplementary data to this article can be found online at https://doi.org/10.1016/j.jechem.2020.06.059.

References

[1] L. Chong, J. Wen, J. Kubal, F.G. Sen, J. Zou, J. Greeley, M. Chan, H. Barkholtz, W. Ding, D.J. Liu, Science 362 (2018) 1276–1281.
[2] H.T. Chung, D.A. Cullen, D. Higgins, B.T. Sneed, E.F. Holby, K.L. More, P. Zelenay, Science 357 (2017) 479–484.
[3] R. Chattot, O.L. Bacq, V. Beermann, S. Kuhl, J. Herranz, S. Henning, L. Kuhn, T. Asset, L. Guetaz, G. Renou, J. Drnec, P. Bordet, A. Pasturel, A. Eychmuller, T.J. Schmidt, P. Strasser, L. Dubau, F. Maillard, Nat. Mater. 17 (2018) 827–833.
[4] M.C. Luo, Y.N. Qin, Y.J. Sun, Y. Yang, D. Wu, S.J. Guo, Acta Phys. -Chim. Sin. 34 (2018) 361–376.
[5] J.Y. Cheon, J.H. Kim, J.H. Kim, K.C. Goddeti, J.Y. Park, S.H. Joo, J. Am. Chem. Soc. 136 (2014) 8875–8878.
[6] J.C. Li, X.P. Qin, P.X. Hou, M. Cheng, C. Shi, C. Liu, H.M. Cheng, M.H. Shao, Carbon 147 (2019) 303–311.
[7] S. Akula, S.G. Peera, A.K. Sahu, J. Am. Chem. Soc. 166 (2019) F897–F905.
[8] H.J. Cui, M.G. Jiao, Y.N. Chen, Y.B. Guo, L.P. Yang, Z.J. Xie, Z. Zhou, S.J. Guo, Small Method 2 (2018) 1800144.
[9] J.M. Luo, X.L. Tian, J.H. Zeng, Y.W. Li, H.Y. Song, S.J. Liao, ACS Catal. 6 (2016) 6165–6174.
[10] Y.C. Fan, S. Ida, A. Staykov, T. Akbay, H. Hagiwara, J. Matsuda, K. Kaneko, T. Ishihara, Small 13 (2017) 1700099.
[11] X.Z. Cui, L. Meng, X.H. Zhang, X.G. Wang, J.L. Shi, Electrochim. Acta. 295 (2019) 384–392.
[12] S. Ratso, M. Kaarik, M. Kook, P. Paiste, V. Kisand, S. Vlassov, J. Leis, K. Tammeveski, Chem. Electro. Chem. 5 (2018) 1827–1836.
[13] C.X. Zhao, B.Q. Li, J.N. Liu, J.Q. Huang, Q. Zhang, Chin. Chem. Lett. 30 (2019) 911–914.
[14] C.J. Kaminsky, J. Wright, Y. Surendranath, ACS Catal. 9 (2019) 3667–3671.
[15] T. He, B. Ni, Y.C. Ou, H.F. Lin, S.M. Zhang, C.Z. Li, J. Zhuang, W.P. Hu, X. Wang, Small Methods 2 (2018) 1800068.
[16] Y. Zhou, Y.F. Xing, J. Wen, H.B. Ma, F.B. Wang, X.H. Xia, Chin. Sci. Bull. 64 (2019) 1158–1166.
[17] A.J. Therrien, A.J.R. Hensley, M.D. Marcinkowski, R.Q. Zhang, F.R. Lucci, B. Coughlin, A.C. Schilling, J.S. McEwen, E.C.H. Sykes, Nat. Catal. 1 (2018) 192–198.
[18] L. Nie, D.H. Mei, H.F. Xiong, B. Peng, Z.B. Ren, X.I.P. Hernandez, A. DeLaRiva, M. Wang, M.H. Engelhard, L. Kovarik, A.K. Datye, Y. Wang, Science 358 (2017) 1419–1423.
[19] Z.L. Zhang, Y.H. Zhu, H. Asakura, B. Zhang, J.G. Zhang, M.X. Zhou, Y. Han, T. Tanaka, A.A. Wang, T. Zhang, N. Yan, Nat. Commun. 8 (2017) 16100.
[20] P. Zhou, X.G. Hou, Y.G. Chao, W.X. Yang, W.Y. Zhang, Z.J. Mu, J.P. Lai, F. Lv, K. Yang, Y.X. Liu, J. Li, J.Y. Ma, J. Luo, S.J. Guo, Chem. Sci. 10 (2019) 5898–5905.
[21] L. Zhao, Y. Zhang, L.B. Huang, X.Z. Liu, Q.H. Zhang, C. He, Z.Y. Wu, L.J. Zhang, J.P. Wu, W.L. Yang, L. Gu, J.S. Hu, L.J. Wan, Nat. Commun. 10 (2019) 1278.
[22] Q.H. Yang, C.C. Yang, C.H. Lin, H.L. Jiang, Angew. Chem. Int. Ed. 58 (2019) 3511–3515.
[23] Z. Zhang, J.P. Xiao, X.J. Chen, S. Yu, L. Yu, R. Si, Y. Wang, S.H. Wang, X.G. Meng, Y. Wang, Z.Q. Tian, D.H. Deng, Angew. Chem. Int. Ed. 57 (2018) 16339–16342.
[24] W. Liu, L.L. Cao, W.R. Cheng, Y.J. Cao, X.K. Liu, W. Zhang, X.L. Mou, L.L. Jin, X.S. Zheng, W. Che, Q.H. Liu, T. Yao, S.Q. Wei, Angew. Chem. Int. Ed. 56 (2017) 9312–9317.
[25] Y. Pan, S.J. Liu, K. Sun, X. Chen, B. Wang, K.L. Wu, X. Cao, W.C. Cheong, R. Shen, A.J. Han, Z. Chen, L.R. Zheng, J. Luo, Y. Lin, Y.Q. Liu, D.S. Wang, Q. Peng, Q. Zhang, C. Chen, Y.D. Li, Angew. Chem. Int. Ed. 57 (2018) 8614–8618.
[26] P. Zhou, N. Li, Y.G. Chao, W.Y. Zhang, F. Lv, K. Wang, W.X. Yang, P. Gao, S.J. Guo, Angew. Chem. Int. Ed. 131 (2019) 14322–14326.
[27] M. Kiani, J. Zhang, Y. Luo, C.P. Jiang, J.L. Fan, G. Wang, J.W. Chen, R.L. Wang, J. Energy Chem. 27 (2018) 1124–1139.
[28] L. Wang, X. Wan, S.Y. Liu, L. Xu, J.L. Shui, J. Energy Chem. 39 (2019) 77–87.
[29] T. Hao, C. Zhang, P.P. Su, Z.F. Shen, H. Liu, G.X. Wang, S.M. Liu, J. Liu, J. Energy Chem. 40 (2020) 137–143.
[30] Z.P. Chen, E. Vorobyeva1, S. Mitchell, E. Fako, M.A. Ortuño, N. López, S.M. Collins, P.A. Midgley, S. Richard, G. Vilé, J.P. Ramírez, Nat. Nanotechnol. 13 (2018) 702–708.
[31] X.J. Zeng, J.L. Shui, X.F. Liu, Q.T. Liu, Y.C. Li, J.X. Shang, L.R. Zheng, R.H. Yu, Adv. Energy Mater. 8 (2018) 1701345.
[32] F.L. Meng, H.X. Zhong, D. Bao, J.M. Yan, X.B. Zhang, J. Am. Chem. Soc. 138 (2016) 10226–10231.
[33] H.L. Fei, J.C. Dong, Y.X. Feng, C.S. Allen, C.Z. Wan, B. Volosskiy, M.F. Li, Z.P. Zhao, Y.L. Wang, H.T. Sun, P.F. An, W.X. Chen, Z.Y. Guo, C. Lee, D.L. Chen, I. Shakir, M.J. Liu, T.D. Hu, Y.D. Li, A.I. Kirkland, X.F. Duan, Y. Huang, Nat. Catal. 1 (2018) 63–72.
[34] Y.F. Chen, Z.J. Li, Y.B. Zhu, D.M. Sun, X.E. Liu, L. Xu, Y.W. Tang, Adv. Mater. 31 (2019) 1806312.
[35] H.X. Xu, D.J. Cheng, D.P. Cao, X.C. Zeng, Nat. Catal. 1 (2018) 339–348.
[36] Y.J. Chen, S.F. Ji, C. Chen, Q. Peng, D.S. Wang, Y.D. Li, Joule 2 (2018) 1242–1264.
[37] Z.H. Li, M.F. Shao, L. Zhou, R.K. Zhang, C. Zhang, M. Wei, D.G. Evans, X. Duan, Adv. Mater. 28 (2016) 2337–2344.
[38] Y.L. Zhang, Z.J. Mu, C. Yang, Z.K. Xu, S. Zhang, X.Y. Zhang, Y.J. Li, J.P. Lai, Z.H. Sun, Y. Yang, Y.G. Chao, C.J. Li, X.X. Ge, W.X. Yang, S.J. Guo, Adv. Funct. Mater. 28 (2018) 1707578.
[39] Y.L. Zhang, Z.J. Mu, J.P. Lai, Y.G. Chao, Y. Yang, P. Zhou, Y.J. Li, W.X. Yang, Z.H. Xia, S.J. Guo, ACS Nano 13 (2019) 2167–2175.
[40] W.X. Yang, Y.L. Zhang, X.J. Liu, L.L. Chen, J.B. Jia, Chem. Commun. 53 (2017) 12934–12937.
[41] M.C. Luo, Z.L. Zhao, Y.L. Zhang, Y.J. Sun, Y. Xing, F. Lv, Y. Yang, X. Zhang, S. Hwang, Y.N. Qin, J.Y. Ma, F. Lin, D. Su, G. Lu, S.J. Guo, Nature 574 (2019) 81–85.
[42] X.X. Huang, Y.L. Zhang, H.M. Shen, W. Li, T. Shen, Z. Ali, T.Y. Tang, S.J. Guo, Q. Sun, Y.L. Hou, ACS Energy Lett. 3 (2018) 2914–2920.
[43] W.X. Yang, Y.L.X. Zhang, J. Liu, L.L. Chen, M.C. Liu, J.B. Jia, Carbon 147 (2019) 83–89.